Electrowetting lattice Boltzmann method for micro- and nano-droplet manipulations

Xin Xu, Fei Wang, Zhangrong Qin,* and Binghai Wen†

Key Lab of Education Blockchain and Intelligent Technology, Ministry of Education, Guangxi Normal University, Guilin 541004, China and Guangxi Key Lab of Multi-Source Information Mining and Security, Guangxi Normal University, Guilin 541004, China

(Received 25 September 2022; accepted 23 March 2023; published 25 April 2023)

Electrowetting has become a widely used tool for manipulating tiny amounts of liquids on surfaces. This paper proposes an electrowetting lattice Boltzmann method for manipulating micro-nano droplets. The hydrodynamics with the nonideal effect is modeled by the chemical-potential multiphase model, in which the phase transition and equilibrium are directly driven by chemical potential. For electrostatics, droplets in the micro-nano scale cannot be considered as equipotential as macroscopic droplets due to the Debye screening effect. Therefore, we linearly discretize the continuous Poisson-Boltzmann equation in a Cartesian coordinate system, and the electric potential distribution is stabilized by iterative computations. The electric potential distribution of droplets at different scales suggests that the electric field can still penetrate micro-nano droplets even with the screening effect. The accuracy of the numerical method is verified by simulating the static equilibrium of the droplet under the applied voltage, and the results show the apparent contact angles agree very well with the Lippmann–Young equation. The microscopic contact angles present some obvious deviations due to the sharp decrease of electric field strength near the three-phase contact point. These are consistent with previously reported experimental and theoretical analyses. Then, the droplet migrations on different electrode structures are simulated, and the results show that droplet speed can be stabilized more quickly due to the more uniform force on the droplet in the closed symmetric electrode structure. Finally, the electrowetting multiphase model is applied to study the lateral rebound of droplets impacting on the electrically heterogeneous surface. The electrostatic force prevents the droplets from contracting on the side which is applied voltage, resulting in the lateral rebound and transport toward the side.

DOI: 10.1103/PhysRevE.107.045305

I. INTRODUCTION

When a voltage is applied, the contact angle of the droplet decreases, and a new equilibrium value is reached, i.e., the voltage enhances the wettability of the surface. This phenomenon is known as electrowetting [1]. Electrowetting is one of the broad ways to control the wettability of liquids because of its fast response speed (several milliseconds), large switching range (several tens of degrees), excellent durability (hundreds of thousands of switching cycles), and low energy consumption (10–100 μW) [2]. Since droplets can be separated, merged, produced, and relocated with the assistance of an electric field, electrowetting is playing an increasing role in displays [3], inkjet printing [4–6], digital microfluidics [7–9], and varifocal lenses [10,11].

Studying the physical laws of fluids on the microscale is crucial to applying electrowetting in practice better. However, there are still some unresolved questions about the physical behavior of droplets in the electrowetting system, and experimental work on micro-nano droplets may be expensive and complicated. Therefore, numerical simulation is a useful way to study the behavior of these systems. Some numerical methods have been proposed in recent years, including the molecular dynamics simulations [12,13], the level set method [14,15], finite element method [16], the phase-field approach [17,18], etc.

For conventional computational fluid dynamics (CFD) methods, within the framework of continuum theory, the whole system is described by macroscopic quantities, and the intermolecular structures are ignored. However, the intermolecular forces or disjoining pressure should be considered at the microscale, making the approximation underlying the continuum picture no longer valid [1]. For molecular dynamics, enormous computational demands limit its application on minimal space and time scales. In contrast to the two methods mentioned above, the lattice Boltzmann method (LBM) is an approach between macroscopic and microscopic scales with unique merits. LBM does not depend on continuum theory, and it is efficient in computation and supports parallel calculations. Aminfar *et al.* [19] extended the free-energy model to simulate electrowetting. They proposed a new relation for surface tensions based on the free-energy functional minimization to estimate the contact angle after applying the voltage. Clime *et al.* [20] used the Shan–Chen multiphase model to simulate the fundamental transport processes of droplets in electrowetting-actuated Hele-Shaw cells. Li *et al.* [21] used the Shan–Chen multiphase model to study the electrowetting of electrolyte droplets and flows on flat and rough surfaces. They demonstrated that the external voltage may efficiently regulate the flow across the channel in a rough-wall

*qinzhangrong@gxnu.edu.cn
†oceanwen@gxnu.edu.cn

 ©2023 American Physical Society

channel. Ruiz-Gutierrez *et al.* [22] used the multifield coupled LB equations with a unified form. They applied the method to study the stability and dynamics of a thin dielectric film and found a good match with analytical predictions based on the lubrication theory. Simulations of electrowetting using the lattice Boltzmann method rarely involve droplets at the micro-nano scale. However, current fluid control research is evolving to the scale [23–25]. In addition, the micro-nano droplets will be affected by the length of the Debye screen differently from the macroscopic droplets due to scale effects. Thus, we developed an LBM for electrowetting of micro-nano droplets.

Several multiphase models have been developed by the LBM community, such as color-gradient model [26], pseudopotential model [27,28], free-energy model [29], discrete Boltzmann method [30], etc. The method used in this study is based on the chemical-potential multiphase model developed by Wen *et al.* [31], which directly evaluates the nonideal force by introducing a chemical-potential gradient. The computational efficiency is improved because the calculation of the pressure tensor is avoided. Meanwhile, the chemical-potential multiphase model has been proved to agree with thermodynamic consistency and Galilean invariance. Recently, by introducing a proportional coefficient, Wen *et al.* [32] decoupled the grid space from the momentum space; this promotes the model to achieve very low temperatures and extreme liquid-gas density ratios while the thermodynamic consistency is still preserved.

This paper is organized as follows. In Sec. II, we briefly review the LB equation and the chemical-potential multiphase model. Then a discretization scheme for solving the electric potential of droplets is given. Finally, the governing equations involving electrostatics in the simulation experiments of this study are presented. In Sec. III, we simulate the static equilibrium configuration of the droplet under the action of an applied voltage. The contact angle obtained from the simulation is compared with the famous Lippmann–Young equation to verify the accuracy. The reason why the microscopic contact angle does not conform to the Lippmann–Young equation is analyzed by calculating the electric field strength along the surface profile of the droplet. Then, the migration under the action of the electric field is simulated. The electric potential distribution, electric field strength, and migration speed are studied under different electrode structures. Last, we study the lateral rebound caused by droplets hitting the electrically heterogeneous surface. The relationship between the momentum and the electric potential is calculated and analyzed. Section IV contains some conclusions.

II. LATTICE BOLTZMANN METHOD

A. Multiple-relaxation-time lattice Boltzmann method

The Boltzmann equation is a mathematical description of fluids motion, which uses an average statistical method to describe the macroscopic motion and fluids properties. But the collision term of the equation is a complex calculus form, and solving its exact solution is impractical. The Boltzmann-BGK equation uses a relaxation method to replace the collision term, which can linearize the collision term to significantly reduce the calculation cost and maintain the average feature of the original collision operator [33]. The lattice Boltzmann equation (LBE) is a special discretization format of the Boltzmann-BGK equation [34]. It uses a lattice to discretize the Boltzmann equation, and the lattice model generally determines the velocity of the particles.

Multiple-relaxation-time (MRT) LBE is adopted in this study, and a 2D lattice with nine velocity vectors, so-called D2Q9, is employed. The evolution equation in a time step δt is as follows [35–38]:

$$f_\alpha(\mathbf{x}+\mathbf{e}_\alpha\delta t, t+\delta t) = f_\alpha(\mathbf{x}, t) - \mathbf{M}^{-1}\mathbf{S}[\mathbf{m}-\mathbf{m}^{\mathrm{eq}}], \quad (1)$$

where $f_\alpha(\mathbf{x}, t)$ is the particle distribution function at time t and lattice site $\mathbf{x}$, moving along the direction defined by the discrete velocity vector e_α with $\alpha = 0, \ldots, 8$, $\mathbf{M}$ is an orthogonal transformation matrix used to transform the distribution function into the momentum space, and $\mathbf{M}^{-1}$ is the inverse matrix of $\mathbf{M}$. The transformation matrix $\mathbf{M}$ can be given by [35]

$$\mathbf{M} = \begin{bmatrix} 1 & 1 & 1 & 1 & 1 & 1 & 1 & 1 & 1 \\ -4 & -1 & -1 & -1 & -1 & 2 & 2 & 2 & 2 \\ 4 & -2 & -2 & -2 & -2 & 1 & 1 & 1 & 1 \\ 0 & 1 & 0 & -1 & 0 & 1 & -1 & -1 & 1 \\ 0 & -2 & 0 & 2 & 0 & 1 & -1 & -1 & 1 \\ 0 & 0 & 1 & 0 & -1 & 1 & 1 & -1 & -1 \\ 0 & 0 & -2 & 0 & 2 & 1 & 1 & -1 & -1 \\ 0 & 1 & -1 & 1 & -1 & 0 & 0 & 0 & 0 \\ 0 & 0 & 0 & 0 & 0 & 1 & -1 & 1 & -1 \end{bmatrix}. \quad (2)$$

$\mathbf{m}$ and $\mathbf{m}^{\mathrm{eq}}$ represent the velocity moments of the distribution functions and their equilibria. For the D2Q9, the flowing result can be obtained [35]:

$$\mathbf{m} = \mathbf{M}\mathbf{f} = \mathrm{M}_{\alpha\beta} f_\beta = (\rho, \sigma, \varsigma, j_x, q_x, j_y, q_y, p_{xx}, p_{xy})^{\mathrm{T}}, \quad (3)$$

where $\mathbf{f} = (f_0, f_1, \ldots, f_8)^{\mathrm{T}}$, σ is the energy mode, ς is related to the energy square. The x and y components of the momentum and energy flux are represented by j_x, j_y, q_x, and q_y, respectively, p_{xx} and p_{xy} are associated with the diagonal and off-diagonal components of the stress tensor. The superscript "T" denotes the transposition operator. $\mathbf{S}$ is a diagonal matrix composed of multiple relaxation times given by [39]

$$\mathbf{S} = \mathrm{diag}(s_\rho, s_\sigma, s_\varsigma, s_j, s_q, s_j, s_q, s_\upsilon, s_\upsilon), \quad (4)$$

where $s_\rho = s_j = 1$, $s_\sigma = 1.64$, $s_\varsigma = 1.54$, $s_q = 1.7$ and $s_\upsilon = 1/\tau$, respectively [35]. τ is related to the viscosity υ:

$$\upsilon = \left(\tau - \tfrac{1}{2}\right)c_{\mathrm{s}}^2\delta t, \quad (5)$$

where the sound speed is $c_{\mathrm{s}} = c/\sqrt{3}$, and $c = \delta x/\delta t$ (the lattice constant $c = 1$). The density ρ and macroscopic velocity $\mathbf{u}$ are calculated by

$$\rho = \sum_{\alpha=0}^{8} f_\alpha, \quad \rho\mathbf{u} = \sum_{\alpha=0}^{8} \mathbf{e}_\alpha f_\alpha. \quad (6)$$

B. Chemical-potential multiphase model

In this study, the entire evolution space contains the liquid phase where the droplet is located and the gas phase around the droplet. For the modeling of multiphase fluids, it

is necessary to ensure that the model can describe the gas-liquid two-phase balance of the multiphase flow movement in actual physical space. The multiphase flow modeling by the chemical-potential multiphase model is divided into two substeps. First, the nonideal force of the multiphase flow is calculated by the chemical-potential gradient; second, the nonideal force is coupled with the LBE.

Following the classic capillary theory of van der Waals (VDW), the free-energy functional within the gradient square approximation is [29,40]

$$\Psi = \int \left(\psi(\rho) + \frac{\kappa}{2}|\nabla\rho|^2\right)dx, \tag{7}$$

where the first term is the bulk free-energy density at a given temperature with the density ρ. The second term gives the free-energy contribution from density gradients in an inhomogeneous system, where κ is the surface tension coefficient. The chemical potential can be derived from the free-energy density function:

$$\mu = \psi'(\rho) - \kappa\nabla^2\rho. \tag{8}$$

The free-energy function in turn determines the diagonal term of the pressure tensor

$$p = p_0 - \kappa\rho\nabla^2\rho - \frac{\kappa}{2}|\nabla\rho|^2, \tag{9}$$

with the general expression of the equation of state (EOS),

$$p_0 = \rho\psi'(\rho) - \psi(\rho). \tag{10}$$

Substituting Eqs. (8) and (10) into the divergence of the pressure tensor, the nonideal force can be calculated by chemical potential [29,41]:

$$\mathbf{F} = -\rho\nabla\mu + c_s^2\nabla\rho. \tag{11}$$

The numerical simulations of static and dynamic fluids confirm that gas-liquid two-phase flow modeled by this method conforms to thermodynamic consistency and Galilean invariance [31,32]. The former guarantees that the mathematical model can correctly simulate the phase balance, and the latter is helpful for the model to evolve the motion of the multiphase flow accurately.

For a given EOS p_0, solving Eq. (10), which is a typical one-order linear ordinary differential equation, the general solution for the free-energy density can be obtained:

$$\psi = \rho\left(\int \frac{p_0}{\rho^2}d\rho + C\right), \tag{12}$$

where C is a constant and does not affect the calculation of nonideal force in Eq. (11). The relevant chemical potential can be obtained by using a specific EOS to express p_0 and substituting Eq. (12) into Eq. (8). In this study, Peng–Robinson (PR) EOS is selected which is usually superior in predicting liquid density:

$$p_0 = \frac{\rho RT}{1-b\rho} - \frac{a\alpha(T)\rho^2}{1+2b\rho-b^2\rho^2}, \tag{13}$$

where R is the universal gas constant, a is the attraction parameter, b is the volume correction, and $\alpha(T) = [1 + (0.37464 + 1.54226\omega - 0.26992\omega^2)(1 - \sqrt{T/T_c})]^2$, where ω is the acentric coefficient. Its chemical potential is [31]

$$\mu = RT\ln\frac{\rho}{1-b\rho} - \frac{a\alpha(T)}{2\sqrt{2}b}\ln\frac{\sqrt{2}-1+b\rho}{\sqrt{2}+1-b\rho} + \frac{RT}{1-b\rho} - \frac{a\alpha(T)\rho}{1+2b\rho-b^2\rho^2} - \kappa\nabla^2\rho. \tag{14}$$

In the following simulations, the parameters are $a = 2/49$, $b = 2/21$, $R = 1$, and $\omega = 0.344$. The reduced variables $T_r = T/T_c$ and $\rho_r = \rho/\rho_c$ are defined to associate the numerical results with the actual physical properties, where the critical temperature $T_c = 4/7$ and the critical density $\rho_c = 7/2$.

The nonideal force is coupled with the LBE through the force term technique [42,43]:

$$f_\alpha(\mathbf{x} + \mathbf{e}_\alpha\delta t, t + \delta t) = f_\alpha(\mathbf{x}, t) - \mathbf{M}^{-1}\mathbf{S}[\mathbf{m} - \mathbf{m}^{eq}] + F_\alpha. \tag{15}$$

In this study, the method proposed by Kupershtokh *et al.* is adopted. The bulk force term is equal to the difference in the equilibrium distribution function after and before the nonideal force acts on the fluid during a time step [44]:

$$F_\alpha = f_\alpha^{eq}(\rho, \mathbf{u} + \delta\mathbf{u}) - f_\alpha^{eq}(\rho, \mathbf{u}), \tag{16}$$

where $\delta\mathbf{u} = \mathbf{F}\delta t/\rho$. Correspondingly, the macroscopic fluid velocity is redefined as the average momentum after and before the collision [45]:

$$\rho\mathbf{u} = \sum_{\alpha=0}^{8}\mathbf{e}_\alpha f_\alpha + \frac{\mathbf{F}\delta t}{2}. \tag{17}$$

Studies have shown that LBE does not require lattice symmetry and the consistency between computational mesh and momentum space [46,47]. So, a proportionality coefficient is introduced to establish the relationship between the space step in the momentum space and the space step in the computational mesh [32]:

$$\delta\hat{x} = k\delta x. \tag{18}$$

Here, if the dimension of a quantity contains a length unit, then the sign of this quantity in the computational mesh is marked with a superscript. The chemical potential in the computational mesh is evaluated by

$$\hat{\mu} = k^2\psi'(\rho) - \hat{\kappa}\hat{\nabla}^2\rho. \tag{19}$$

Thus, the computational mesh can use more lattices to simulate the gas-liquid transition region to obtain more accurate and stable results when calculating the derivative and gradient (for more details, see the Appendix). A large gas-liquid density ratio can be achieved while conforming to thermodynamic consistency and Galilean invariance.

C. Poisson-Boltzmann equation discretization

Before calculating the contribution of the electric field force to the droplet, the electric potential should be estimated. The Poisson–Boltzmann (PB) equation is used to solve the electric potential distribution of the micro-nano droplet. It is a functional equation that aims to describe the electric potential

distribution of the solution in the direction normal to a charged surface.

For a solution containing ion i (the valence is z_i), the static charge density at $\mathbf{x}$ is expressed as $z_i e\rho_i$, where e is electronic charge. Then the Boltzmann distribution equation of ion i is

$$\rho_i = \rho_{\infty i} e^{-z_i e\varphi/k_B T}, \tag{20}$$

where the $\rho_{\infty i}$ is the ion concentration at the bulk, φ is electric potential, and k_B is the Boltzmann constant. Another essential equation that needs to be satisfied is the Poisson equation for the net external charge density at $\mathbf{x}$:

$$\frac{d^2\varphi}{d\mathbf{x}^2} = -\sum_i \frac{z_i e\rho_i}{\varepsilon_0 \varepsilon_r}, \tag{21}$$

where ε_0 is vacuum dielectric constant, and ε_r is relative permittivity dielectric constant. Substituting Eq. (20) into Eq. (21), the PB equation can be obtained [48]:

$$\frac{d^2\varphi}{d\mathbf{x}^2} = -\sum_t \left(\frac{z_i e\rho_{\infty i}}{\varepsilon_0 \varepsilon_r}\right) e^{-z_i e\varphi/k_B T}. \tag{22}$$

The electric potential distribution inside the droplet must satisfy the PB equation. For the electrolyte solutions with one-to-one valence, the nonlinear PB equation can be rewritten as

$$\frac{d^2\varphi}{d\mathbf{x}^2} = \frac{e\rho_\infty}{\varepsilon_0 \varepsilon_r}(e^{e\varphi/k_B T} - e^{-e\varphi/k_B T}). \tag{23}$$

When the applied voltage is less than 1, Eq. (23) can be linearized [19]:

$$\frac{d^2\varphi}{d\mathbf{x}^2} = \frac{2e^2\varphi\rho_\infty}{\varepsilon_0 \varepsilon_r k_B T}. \tag{24}$$

An important parameter is the so-called Debye screening constant κ_D, which describes the exponential attenuation of the electric potential in the solution:

$$\kappa_D^2 = \frac{2e^2\rho_\infty}{\varepsilon_0 \varepsilon_r k_B T} = \frac{1}{l_D^2}, \tag{25}$$

where l_D is the Debye length. Since the droplet size is small, the effect of Debye length must be considered in the simulation. Substituting Eq. (25) into Eq. (24) gives

$$\frac{d^2\varphi}{d\mathbf{x}^2} = \kappa_D^2 \varphi. \tag{26}$$

Aminfa *et al.* [19] use polar coordinate to discretize and compute Eq. (26), therefore it is not convenient to be applied to the droplet deformation. This paper discretizes the PB equation in the Cartesian coordinates because it is more suitable for dealing with nonsymmetric droplet motion due to nonuniform voltage:

$$\frac{\partial^2\varphi}{\partial x^2} + \frac{\partial^2\varphi}{\partial y^2} = \kappa_D^2 \varphi. \tag{27}$$

Through the central difference scheme of the second-order derivative in two dimensions and four times relationship between ω_{1-4} and ω_{5-8} in D2Q9, taking $\delta x = \delta y$, the central difference scheme of the second-order derivative in two-dimensional can be obtained:

$$\nabla^2\varphi_{i,j} = \frac{2}{3\delta x^2}(\varphi_{i,j+1} + \varphi_{i,j-1} + \varphi_{i+1,j}\varphi_{i-1,j}) - \frac{4}{\delta x^2}\varphi_{i,j} + \frac{1}{3\delta x^2}(\varphi_{i+1,j+1} + \varphi_{i+1,j-1} + \varphi_{i-1,j+1}\varphi_{i-1,j-1}). \tag{28}$$

Substituting Eq. (28) into Eq. (27), the discrete PB equation can be obtained:

$$\frac{2}{3\delta x^2}(\varphi_{i+1,j} + \varphi_{i-1,j} + \varphi_{i,j+1} + \varphi_{i,j-1}) - \frac{4}{\delta x^2}\varphi_{i,j} + \frac{1}{3\delta x^2}(\varphi_{i+1,j+1} + \varphi_{i-1,j-1} + \varphi_{i-1,j+1} + \varphi_{i+1,j-1}) = \kappa_D^2 \varphi_{i,j}. \tag{29}$$

The discrete PB equation gives

$$\varphi_{i,j} = \frac{1}{4 + \kappa_D^2 \delta x^2}\left[\frac{2}{3}(\varphi_{i+1,j} + \varphi_{i-1,j} + \varphi_{i,j+1} + \varphi_{i,j-1}) + \frac{1}{3}(\varphi_{i+1,j+1} + \varphi_{i-1,j-1} + \varphi_{i-1,j+1} + \varphi_{i+1,j-1})\right]. \tag{30}$$

The electric potential can be obtained by solving Eq. (30) with Jacobi iteration.

D. Governing equations for the electrostatic field

The areas of conductive droplets and insulating fluid are marked as Ω_1 and Ω_2, respectively. In addition, the gas-liquid interface, the solid-liquid interface, and the solid-gas interface are denoted by Γ_{lg}, Γ_{sl}, and Γ_{sg}, respectively. $\mathbf{n}$ represents the normal unit vector from Γ_{lg} to Ω_2.

For electrostatics, a constant electric potential U is applied to the substrate. The electric potential in the region Ω_1, as described in Sec. II, satisfies the PB equation. In the Ω_2, the electric potential satisfies the Laplace equation:

$$\nabla^2\varphi = \frac{\partial^2\varphi}{\partial x^2} + \frac{\partial^2\varphi}{\partial y^2} = 0. \tag{31}$$

The permittivity of the liquid phase is much larger than that of the gas phase. So the following condition can be assumed at Γ_{lg} [49]:

$$\mathbf{n} \cdot \nabla\varphi = 0. \tag{32}$$

According to the Gauss law, the relationship between electric potential and free charge ρ_e can be obtained [50]:

$$\varepsilon_0 \nabla \cdot (\varepsilon_r \nabla\varphi) = -\rho_e. \tag{33}$$

The electric field strength can be regarded as a gradient of the electric potential, $\mathbf{E} = -\nabla\varphi$. So that the total force can be calculated by

$$\mathbf{F} = -\rho\nabla\mu + c_s^2\nabla\rho + \varepsilon_0\nabla\cdot(\varepsilon_r\nabla\varphi)\nabla\varphi - \frac{\varepsilon_0}{2}(\nabla\varphi)^2\nabla\varepsilon_r, \tag{34}$$

where the third term on the right side of the Eq. (34) is Coulombic force and the fourth term is polarization stress [51]. The solution of derivative is used the fourth-order central

difference. Specifically, the solution of electric potential is used second-order central difference to improve the efficiency of the iterative calculation. The ε_r can be expressed as [52]

$$\varepsilon_r = \frac{\rho - \rho_l}{\rho_g - \rho_l}\varepsilon_g - \frac{\rho - \rho_g}{\rho_l - \rho_g}\varepsilon_l, \tag{35}$$

where ε_g and ε_l are the relative permittivities of gas and liquid, respectively. ρ_g and ρ_l are the coexistence densities obtained by the Maxwell equal-area construction. By coupling the nonideal force and the electrostatic force and acting together on the momentum change of the system, our model can reflect the phase separation and phase balance under the applied voltage. In addition, the Bond number $\mathrm{Bo} = \sqrt{g\Delta\rho r^2/\gamma_{lg}}$ measures the strength of gravity with respect to surface tension, which decreases with the droplet radius reduction. Therefore, the gravity effect in the conditions of micro-nano droplets is neglected in the rest of the paper.

The LBM discretizes the physical space with grids, so the physical quantities in the computational grid are dimensionless. Converting the lattice dimension of physical quantities to the actual dimension should be considered to simulate real-world physical processes. The apostrophe is added to represent physical quantities in the lattice dimension, and without the symbol, physical quantities are expressed using the international system of units. The length dimension L_D, time dimension T_D, mass dimension G_D, and current dimension I_D are defined as follows:

$$\begin{cases} L_D = \frac{r_0}{r_0'} \\ T_D = \frac{\nu'}{\nu} L_D^2 \\ G_D = \frac{\rho}{\rho'} L_D^3 \\ I_D = \frac{U'}{U} L_D^2 G_D T_D^{-3} \end{cases}, \tag{36}$$

where the viscosity coefficient $\nu = 0.01\mathrm{cm}^2/\mathrm{s}$, $\nu' = 0.1$ [calculated by Eq. (5)], and U is the voltage applied on the substrate. The above four quantities are taken as the base dimensions, and the dimensions of all physical quantities in this paper can be derived from their combination. Thus, the dimension conversion can be achieved.

III. RESULTS AND DISCUSSION

In our simulation experiment, a conductive droplet is immersed in another insulating fluid (vapor in this study). A constant voltage is applied on the solid surface to generate an electric field and affect the wetting behavior of the droplet. Zero potential is set at the top boundary of the flow field. The system is in a limited area, where the substrate is x axis. Periodic boundary conditions are adopted in the x-axis direction, and the half-way bounce boundary conditions are imposed on the top and bottom boundaries. The contact angle is a vital feature to reflect the wettability of a solid surface. The chemical-potential multiphase model can effectively simulate wetting phenomena, so a constant chemical potential μ_s is set on the solid surface to characterize the initial contact angle. The density distribution of the flow field is initialized by [53]

$$\rho(x, y) = \frac{\rho_g + \rho_l}{2} + \frac{\rho_g - \rho_l}{2}\tanh\left[\frac{2(r - r_0)}{W}\right], \tag{37}$$

where $W = 10$ is the initial gas-liquid interface width, $r = \sqrt{(x - x_0)^2 + (y - y_0)^2}$, where the node (x_0, y_0) is the center of the droplet, and r_0 is the initial droplet radius. In this study, $T_r = 0.6$, $\tau = 0.8$, $k = 0.2$, $\varepsilon_0 = 8.85 \times 10^{-12}\ \mathrm{C^2\,J^{-1}\,m^{-1}}$, $\varepsilon_l = 81$, $\varepsilon_g = 1$, and the gas-liquid surface tension $\gamma_{lg} = 0.072\mathrm{N/m}$. Unless otherwise indicated, $l_D = 9.6$ nm [54], the macroscopic size of the droplet is 40 nm and r_0 takes 80 lattice units.

The electric potential distribution of the droplet is solved by using the discretized PB equation, and the grid independence is checked. Then an example about droplet spread is used to verify the correctness of the numerical method. Finally, droplet migration and lateral rebound due to the inhomogeneous voltage are simulated.

A. Electric potential distribution inside a droplet

According to Eq. (30), the electric potential $\varphi'_{i,j}$ of the fluid node (i, j) at the next time step is calculated by the one of the neighboring nodes. This iterative process is repeated until the absolute error value of the electric potential between the two-time steps reaches a pre-specified convergence criterion, i.e., $|\varphi_{i,j} - \varphi'_{i,j}| < 10^{-7}$. The electric potential distribution of droplets with different sizes was simulated, and the electric potential variation along the perpendicular bisector was observed. Also, each droplet size was simulated by using different mesh densities to check the grid independence.

For droplets with $r_0 = 10$ nm, 20 nm, and 40 nm as shown in Fig. 1, the electric potential distributions were simulated when the grid sizes are 0.1 nm, 0.2 nm, 0.5 nm, and 1 nm, respectively. The results show that variation in the mesh density has almost no effect on the electric potential distribution. Moreover, it can be seen that the electric potential is attenuated exponentially along the positive direction of the y axis. The electric potential is above 0.3 V for the droplet with $r_0 = 10$ nm [Fig. 1(a)]. Doubling the droplet radius, as shown in Fig. 1(b), the electric double layer (EDL) attenuates the electric potential by up to more than half. By doubling the droplet size again, the electric potential can be attenuated to less than 0.1 V [Fig. 1(c)]. It can be seen that the screening effect becomes more and more significant as the droplet size increases because the EDL described by the PB equation leads to an increasing electrical screening for each additional Debye length from the charged solid surface. The electric potential distribution of the droplet with $r_0 = 1000$ nm is simulated when the grid sizes are 1 nm and 2 nm, respectively. The results are also grid independence. The electric potential can be attenuated to approximate 0 V since the droplet radius is much larger than the l_D.

To show the electric potential distribution of the droplet intuitively, we plotted the electric potential contour diagrams of the droplets with $r_0 = 10$ nm, 20 nm, 40 nm, and 1000 nm, corresponding to Fig. 2, respectively. The electric field penetrates the droplet with $r_0 = 10$ nm due to its miniature size, although it is affected by the screening effect [Fig. 2(a)]. The proportion of voltages above 0.3 V is less as the droplet size increases [Figs. 2(b) and 2(c)]. For the droplet with $r_0 =$ 1000 nm, most of the electric potential is close to 0 V, and the EDL nearly screens the external electric field [Fig. 2(d)]. It indicates that electric fields penetrate micro-nano droplets,

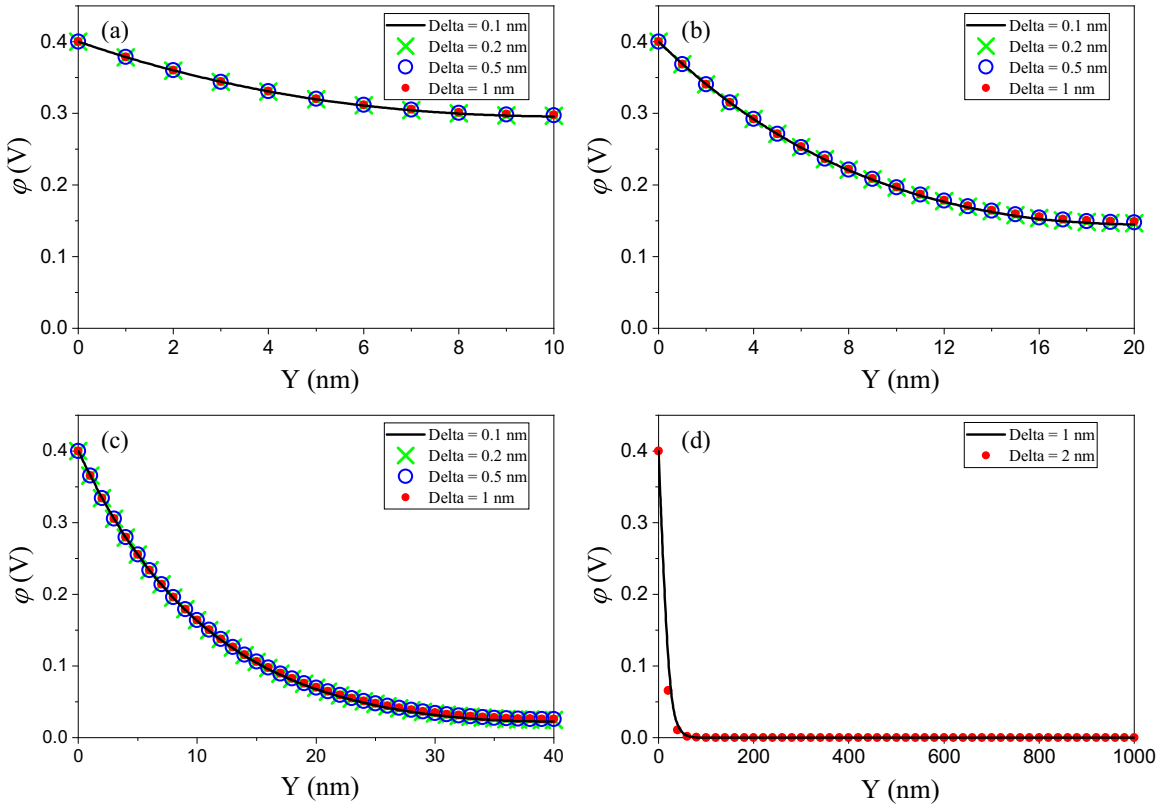

FIG. 1. The electric potential variations at the perpendicular bisector of the droplet: (a) $r_0 = 10$ nm, (b) $r_0 = 20$ nm, (c) $r_0 = 40$ nm, and (d) $r_0 = 1000$ nm. The Debye screening causes the exponential reduction in electric potential. Electric potential variations are the same with a given droplet radius regardless of the mesh density, suggesting that the results are grid independence.

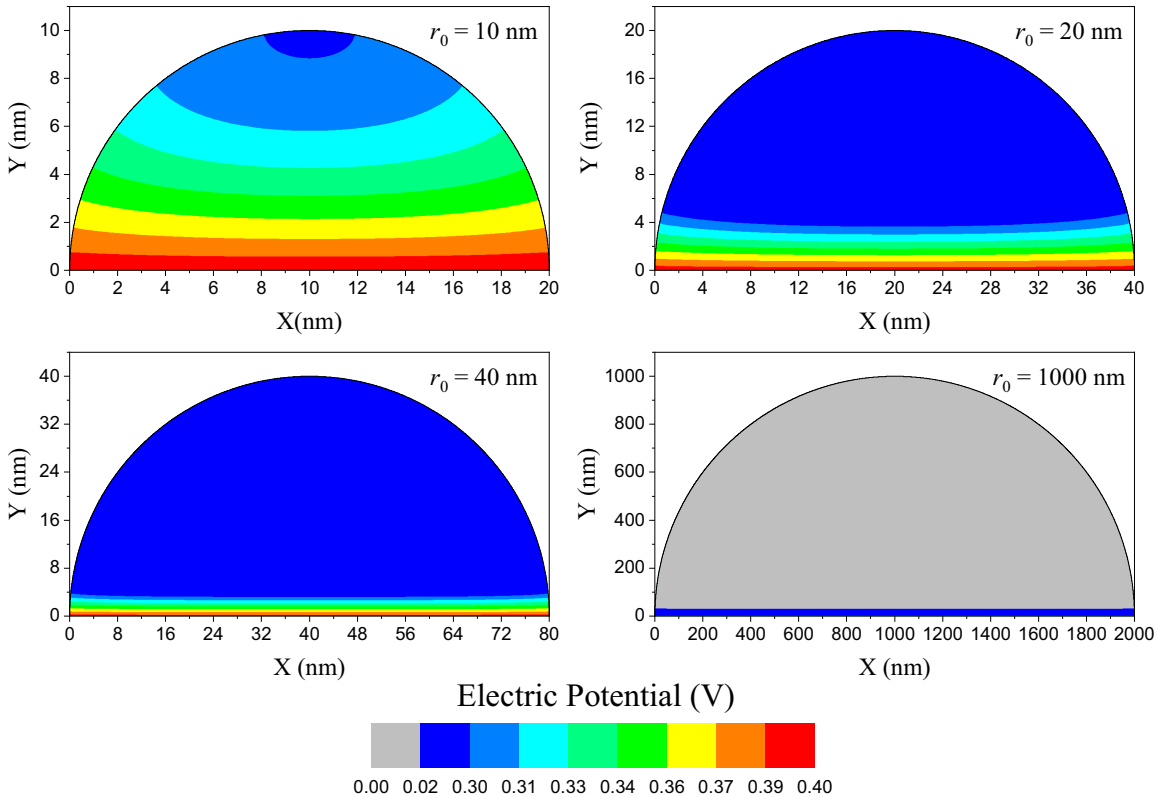

FIG. 2. The electric potential distribution of the droplet: $r_0 = 10$ nm, 20 nm, 40 nm and 1000 nm. As the radius increases, it becomes progressively difficult for the electric field to penetrate through the entire droplet.

unlike macroscopic droplets that can be considered equipotential bodies.

B. Equilibrium configuration of a droplet in electric fields

After obtaining the electric potential, this section verified the accuracy of the simulation method by simulating the static equilibrium configuration of a droplet under the applied voltage and compared the contact angle obtained from the simulation with the well-known Lippmann–Young equation [55].

Without applying voltage, the droplet on the substrate satisfies the Young equation:

$$\cos\theta_{\mathrm{Y}} = \frac{\gamma_{\mathrm{sg}} - \gamma_{\mathrm{sl}}}{\gamma_{\mathrm{lg}}}, \tag{38}$$

where θ_{Y} denotes Young's contact angle, and γ_{sg} and γ_{sl} represent the surface tension at Γ_{sg} and Γ_{sl}, respectively. When voltage is applied to the substrate, the horizontal component of the electrostatic force acting on the droplet surface breaks the balance of forces, causing the droplet to spread, and the apparent contact angle θ satisfies the following equation:

$$\cos\theta = \frac{\gamma_{\mathrm{sg}} - \left(\gamma_{\mathrm{sl}} - \frac{\varepsilon_0\varepsilon_{\mathrm{r}}}{2d}U^2\right)}{\gamma_{\mathrm{lg}}}. \tag{39}$$

Substituting Eq. (38) into Eq. (39), the famous Lippmann-Young equation is obtained:

$$\cos\theta = \cos\theta_{\mathrm{Y}} + \frac{1}{2}\frac{\varepsilon_0\varepsilon_{\mathrm{r}}}{d\gamma_{\mathrm{lg}}}U^2, \tag{40}$$

where d is the fixed distance where the counter-ions are all located from the solid surface. This equation describes the relationship between the contact angle and the voltage in the electrowetting model, i.e., the contact angle of the droplet decreases as the applied voltage increases. Additionally, at the same voltage, the contact angle can be varied in a wider range when d is shorter. So d (i.e., l_{D}) takes 2 nm [55] in this section.

The computational domain is a rectangle with a width of 300 lattice units and a height of 150 lattice units. First, the voltage on the substrate is set to 0 V and relax the droplet for 5×10^4 time steps. The droplet will spread on the substrate and eventually stabilize into a spherical cap. Then the voltage was applied, and the contact angle was recorded after relaxation for 5×10^4 time steps.

The contact angle variation results are illustrated in Fig. 3. The apparent contact angle decreases gradually with increasing voltage and agrees with the Lippmann–Young equation. Because the electric field exerts electrostatic traction on Γ_{lg} near the three-phase contact point, resulting in a net force in the direction parallel to the solid surface, leading to a deformation of the droplet surface and a reduction in the apparent contact angle. In contrast, the microscopic contact angle decreases slightly, no longer described by the Lippmann–Young equation, and approaches the angle indicated by the Young equation. This feature was observed experimentally [56] and predicted by the electromechanical model of electrowetting [57]. To better explain this feature, we calculated the electric field strength along the droplet surface and normalized arc length $s \in [0, 1]$, and $s = 0, 1$ correspond to the left and right three-phase contact points, respectively. Figure 4 illustrates that the electric field strength does not simply increase monotonically as the distance from the substrate decreases. In contrast, as s approaches 0 or 1, the electric field strength tends to increase and then decrease sharply. In addition, the inset shows that the maximum value of the electric field strength increases with the increment in the mesh density. The reason is that the electric field strength varies drastically in the tiny area near the three-phase contact points. Therefore, using more points can better capture the electric field intensity variation trends.

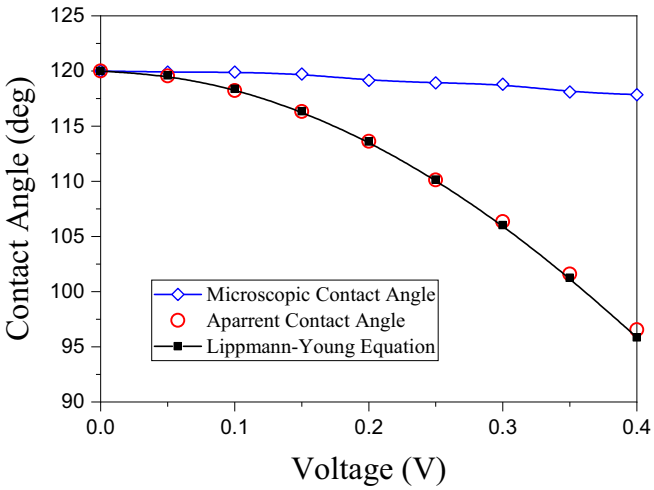

FIG. 3. Comparison of the variation of contact angle with the analytical solution. The apparent contact angle decreases with increasing voltage and is consistent with the Lippmann–Young equation. In contrast, the voltage variation slightly affects the microscopic contact angle.

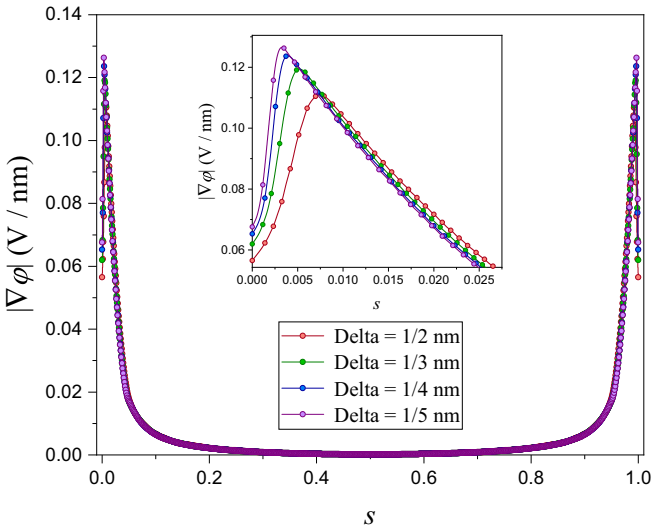

FIG. 4. The electric field strength along the droplet interface in different mesh densities. The inset shows magnified views in $s \in [0, 0.0275]$. When approaching the three-phase contact points, the electric field strength first increases and then decreases sharply. In addition, the electric field strength near the three-phase contact points gradually enhances as the mesh density increases.

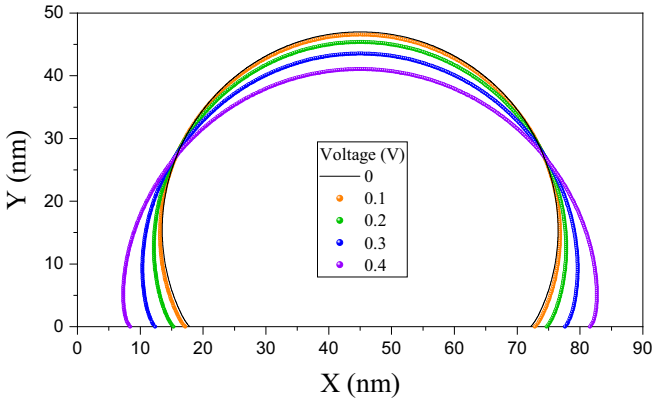

FIG. 5. The variation of droplet contour line with increasing voltage.

From the equilibrium profile of the droplet surface in Fig. 5, it can be seen more intuitively that the electrostatic force drives the droplet to spread compared to the interface profile in the absence of the electric field. And the microscopic contact angle at the three-phase contact point does not change significantly during the droplet spreading process.

C. Droplet migration driven by electrowetting

Electrowetting has been widely applied in digital microfluidics. This section simulated the droplet migration on a solid surface driven by an inhomogeneous electric field. The parameters are chosen as $U = 0.2$ V and $\theta_Y = 120^\circ$.

In digital microfluidics, the electrode array is generally controlled by digital signals to drive the droplet movement.

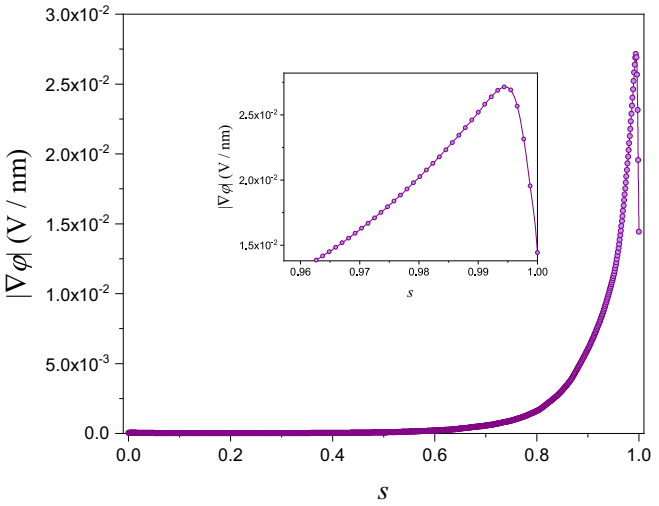

FIG. 7. The electric field strength along the droplet interface in the open structure. The inset shows a magnified view in $s \in [0.89, 1]$.

Therefore, droplet migration in an open electrode structure and closed symmetric electrode structure will be simulated, respectively. The droplet migration simulation in an open structure is shown in Fig. 6. The computational domain is a rectangular flow field with a width of 400 lattice units and a height of 150 lattice units. The electrode length is 50 nm, and the electrode is located between 50 nm and 100 nm. The electrode covers 25% of the solid-liquid interface in the initial phase. Figure 7 shows the electric field strength at the gas-liquid interface of the droplet in the initial state, and $s = 0, 1$ represent the three-phase contact points on the left and right

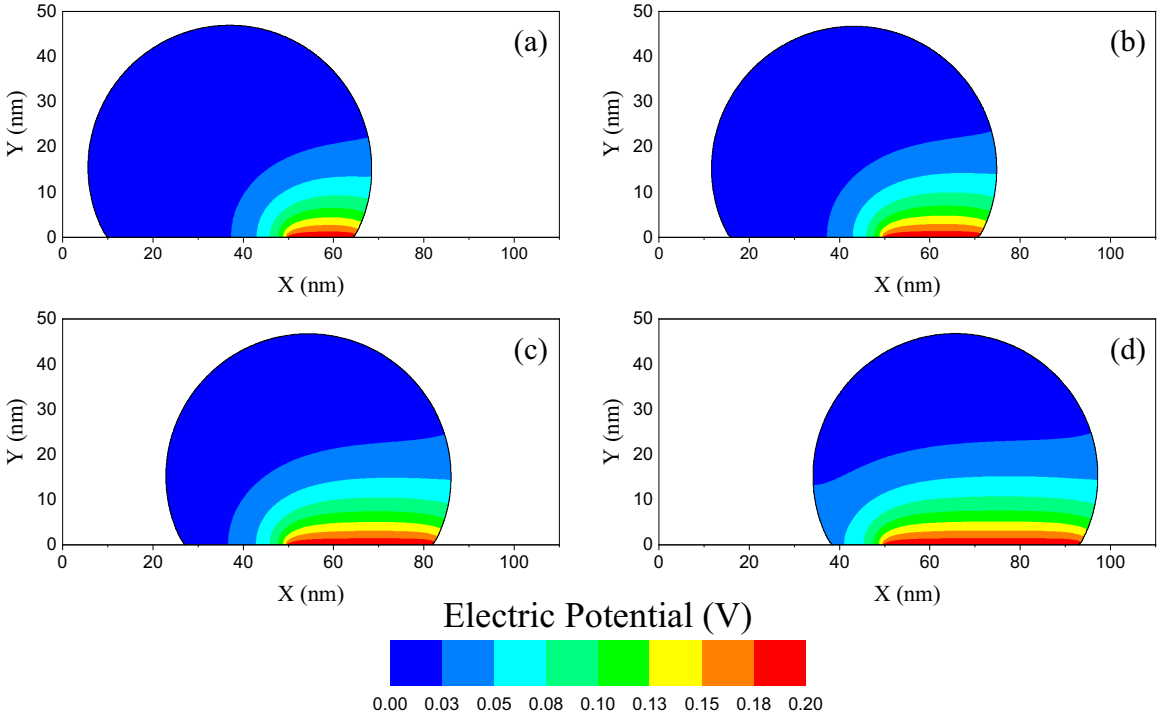

FIG. 6. The electric potential distribution of the drop during the migration process in an open structure: (a) $t = 0.05$ ns, (b) $t = 1$ ns, (c) $t = 2$ ns, and (d) $t = 3$ ns.

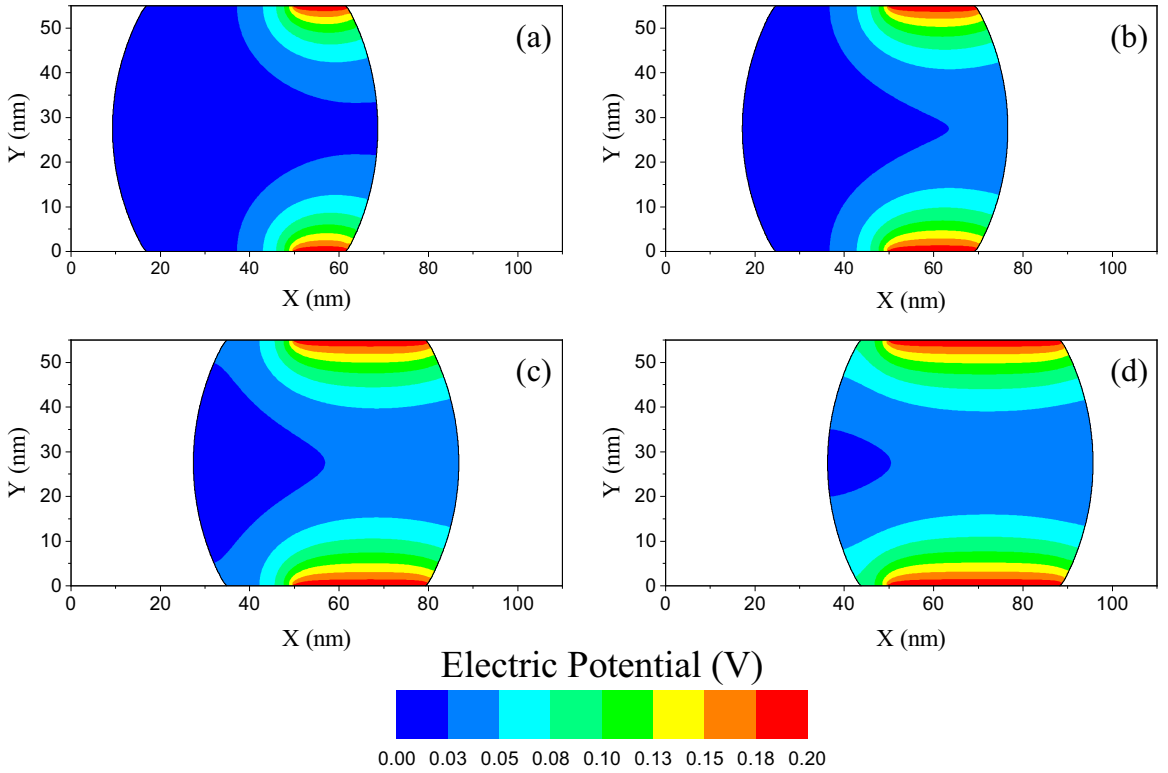

FIG. 8. The electric potential distribution of the droplet during the migration process in the closed symmetric electrode structure: (a) $t = 0.05$ ns, (b) $t = 1$ ns, (c) $t = 2$ ns, and (d) $t = 3$ ns.

sides of the droplet, respectively. Because the left side of the droplet is not in touch with the electrode, the electric field strength at $s = 0$ is approximate 0 V/nm. As s increases, the electric field strength enhances, and the electric force on the right side is considerably larger than that on the left, causing the droplet to migrate to the right. The contact length between the droplet and the electrode steadily increases as the droplet moves rightward. The electrode begins to affect the left part of the droplet, which shows the same step-like electric potential attenuation pattern as the right.

The closed structure is more difficult to manufacture than the open structure, but it prevents the droplets from evaporating and contaminating. Figure 8 shows the simulation results for the closed symmetric electrode structure. The computational domain is a rectangular flow field with 400 lattice units for width and 114 lattice units for height. The 50-nm-long electrodes on both the top and bottom plates locate from 50 nm to 100 nm, and the spacing between them is 55 nm. The electrode initially covers about a quarter of the solid-liquid interface. The electric potential distribution is also symmetrical up and down due to the symmetry in the electrode configuration. Figure 9 depicts the electric field strength at the right gas-liquid interface in the initial phase. $s = 0, 1$ represent the right three-phase contact point located at the top and bottom plates, respectively. Similarly, the electric field strength is symmetrically distributed at the gas-liquid interface. It is lowest (around 3.2×10^{-3} V/nm) in the middle of the two plates and gradually increases from the center to the two sides, reaching a maximum (about 2.7×10^{-2} V/nm).

The migration speed during droplet movement is generally the main focus of studies. The aim is to comprehend transport dynamics and consequently increase transportation efficiency. The following study will analyze the average speed of droplet migration in an open structure and a closed symmetric structure, respectively. The three-phase contact points on the left and right sides of the open structure are marked by the A and B, respectively. Due to the symmetry of the top and bottom planes in the closed structure, only the three-phase contact points on the left and right sides at the lower boundary are observed, marked by the C and D, respectively.

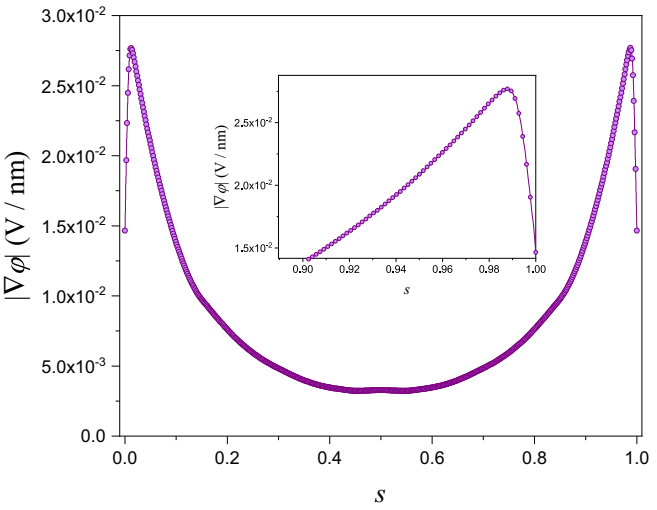

FIG. 9. The electric field strength along the droplet interface in the closed symmetric electrode structure. The inset shows a magnified view in $s \in [0.96, 1]$.

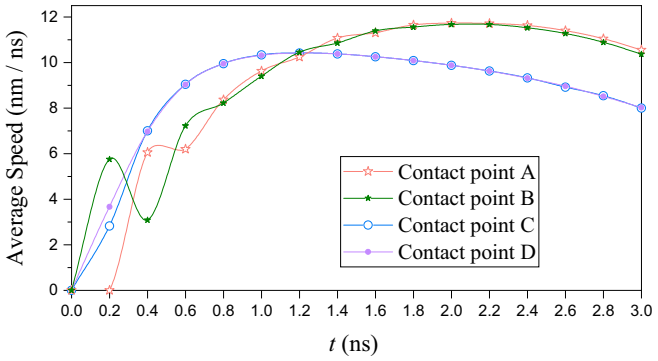

FIG. 10. The average speed of each three-phase contact point during droplet migration in different structures.

The average speed of the four contact points throughout the droplet migration is shown in Fig. 10. Initially, the droplet is at a standstill, and the average speed of both the four contact points is 0 nm/ns. For the open structure, B accelerates to 5.8 nm/ns in the first period due to electric force acting on the right side of the droplet. In contrast, A remains stationary because the moving distance of B is insufficient to cause the right side of the droplet to pull A. In the second period, the right side of the droplet starts to pull the left side to move, while the left side will prevent the rightward movement due to the reaction force. Therefore, the average speed of A exceeds that of B and reaches 6 nm/ns, while the average speed of B drops to 3.1 nm/ns. Similarly, in the third period, the combined effect from the rightward push and the electric force results in the speed of B (7.2 nm/ns) exceeding that of A (6.2 nm/ns). Throughout the process, the speeds of A and B alternately exceed each other, and the droplet speed shows an overall increasing trend. The speed differential between A and B gradually decreases, eventually tending to nearly the same speed.

For the closed symmetric structure, also in the first period, the average speed of D reaches 3.7 nm/ns, which is higher than the average speed 2.8 nm/ns at C due to the electric force. However, compared to the open structure, there is almost no difference between the speed of C and D in the second period, which reaches about 7 nm/ns. Following that, the two points keep moving at about the same speed. The two contact points in the closed symmetric structure are faster than those in the open structure from the second to the fifth periods. While the difference in electric field strength near the three-phase contact point is minimal, as shown in Figs. 7 and 9, the open structure primarily acts on the bottom part of the droplet. In contrast, the closed symmetric structure simultaneously acts on both the top and bottom parts. Additionally, since the force on the droplet is more uniform in the closed structure than in the open structure, the speed of the entire droplet can be stabilized more quickly.

It is notable that the acceleration of C and D gradually decreases, and the average speed of both C and D starts to fall after reaching 10.4 nm/ns in the sixth period. Because as C gradually approaches the electrode, the electric potential on the left side begins to increase. The leftward electric force prevents the droplet from moving to the right. Similarly, after attaining the 11.7 nm/ns in the 11th period, the average speed of A and B begin to drop. Through numerical simulation, it is available to observe the speed fluctuation at the three-phase contact point over time, which aids in selecting optimal parameters for more precise control of droplet migration speed in real applications.

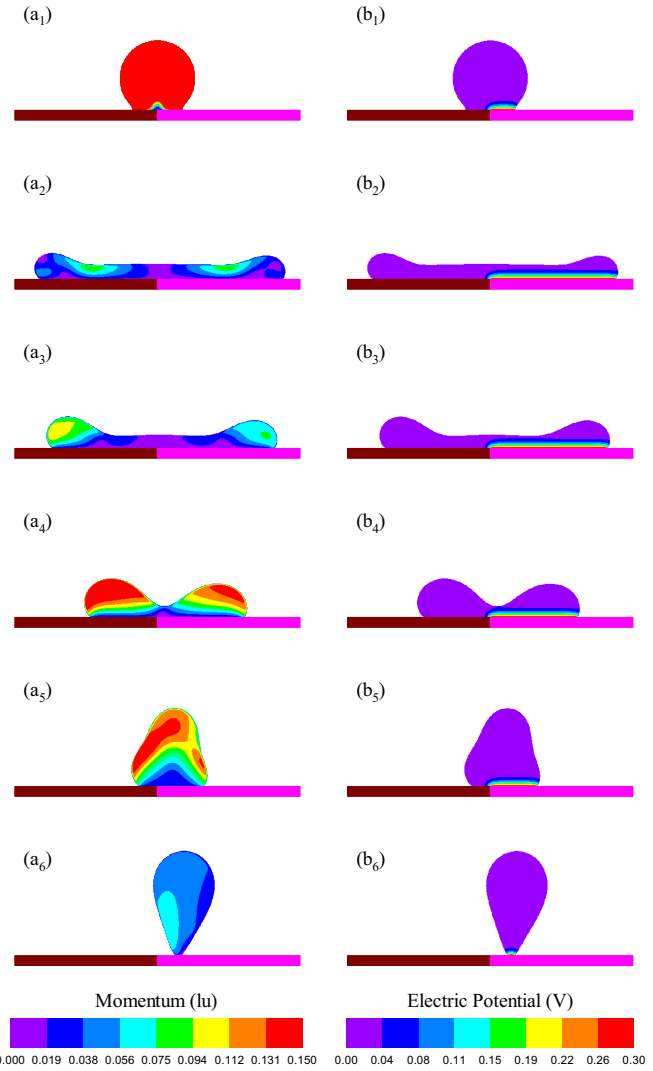

FIG. 11. The distribution of momentum modulus and electric potential inside the droplet during the impact: (a_1, b_1) $t = 0.16$ ns, (a_2, b_2) $t = 1.4$ ns, (a_3, b_3) $t = 1.95$ ns, (a_4, b_4) $t = 2.89$ ns, (a_5, b_5) $t = 3.98$ ns, and (a_6, b_6) $t = 5.17$ ns.

D. Drop lateral rebound induced by electrowetting

Droplet bouncing has many engineering applications, such as self-cleaning and surface cooling. In the last example, a voltage is applied on the right side of the solid surface to simulate the lateral rebound of the droplet after it hits the surface, which can be used to extend the bouncing application. The macroscopic size of the droplet is 100 nm and r_0 takes 80 lattice units. The other parameters are chosen as $U = 0.4$ V and $\theta_Y = 150^\circ$. The computational domain is a rectangle with a width of 720 lattice units and a height of 300 lattice units, and the droplet center is at (360, 130). The droplet hits the solid surface with the velocity of 0.06.

The droplet rebound is usually characterized by two processes, diffusion and recoil, as it impacts a solid surface. To further understand the intrinsic mechanism during the droplet impact on the electrically heterogeneous surface, we plotted the momentum modulus distribution of the droplet and the corresponding electric potential distribution. First, the droplet spreads rapidly, and its kinetic energy is partially converted into surface energy [Figs. 11(a_1)–11(a_2)]. The spreading speed of the droplet gradually decreases under various resistances during spreading [Figs. 11(a_3)–11(a_4)]. The droplet retracts to reduce its interfacial energy when it spreads to the maximum distance. The droplet has enough energy to rebound if the dissipation within the droplet and the friction with the surface are small enough. If there is no voltage applied, then the droplet is symmetric throughout the spreading and retraction process, the internal momentum modulus change is symmetrical, and the center of mass does not deviate from the centerline of the substrate. The electric field produces electrostatic traction on the right side of the droplet when voltage is applied to the right side of the solid surface. It causes the droplet to have a rightward acceleration, preventing the right side from contracting and causing the left side of the droplet to contract faster than the right. As a result, the internal momentum modulus shows an asymmetric distribution, and the center of mass deviates from the centerline of the substrate, resulting in the lateral rebound. Through numerical simulation, the relationship between the momentum distribution and the electric potential distribution at each moment of the rebound process can be easily and quantitatively analyzed to reveal the law of motion [Figs. 11(a_5)–11(a_6)].

IV. CONCLUSION

In this paper, we have presented an electrowetting lattice Boltzmann method to simulate the behaviors of micro-nano droplets in an electrostatic field. The chemical-potential multiphase model is used to simulate phase transition and equilibrium, making the system thermodynamically consistent and Galilean invariant. For electrostatics, droplets in the micro-nano scale cannot be considered as equipotential as macroscopic droplets due to the Debye screening effect. Thus, the nonlinear continuous PB equation, a tool to describe the EDL, is linearized and discretized in the Cartesian coordinate system to iteratively calculate the electric potential. The total force obtained by coupling the gradient of chemical potential and electric potential is applied to the momentum variation of the system through the force term technique.

Through simulations of the electric potential distribution of droplets with different sizes, it is observed that the electric potential is attenuated exponentially when away from the charged substrate. Moreover, the micro-nano droplets cannot wholly screen the charge, indicating that the variation of the electric potential inside the droplets should be considered. The grid independence was also demonstrated. Then we have validated the accuracy of the simulation method by simulating the equilibrium configuration of the droplet under the action of an electric field. The results demonstrate that the apparent contact angle agrees with the Lippmann-Young equation. Meanwhile, the microscopic contact angle deviates from this equation and approaches Young's angle. The electric field strength along the droplet profile line was calculated to analyze the reason. The results show that the electric field strength sharply drops when approaching the three-phase contact point, resulting in a less electrostatic effect on the microscopic contact angle. These are consistent with previously reported experimental and theoretical analyses.

We have simulated the droplet migration in the open electrode structure and closed symmetric electrode structure, respectively. The electric potential distribution, electric field strength, and migration speed in the two structures were compared and analyzed. Since the force on the droplet is more uniform in the closed structure than that in the open structure, the speed of the entire droplet can be stabilized more quickly. The simulation enables us to observe the speed variation of the three-phase contact points at different time periods and select suitable parameters to control the drop movement in applications accurately. Finally, the electrowetting multiphase model is applied to study the lateral rebound of droplets impacting on an electrically inhomogeneous surface. The droplet momentum and the corresponding electric potential distribution

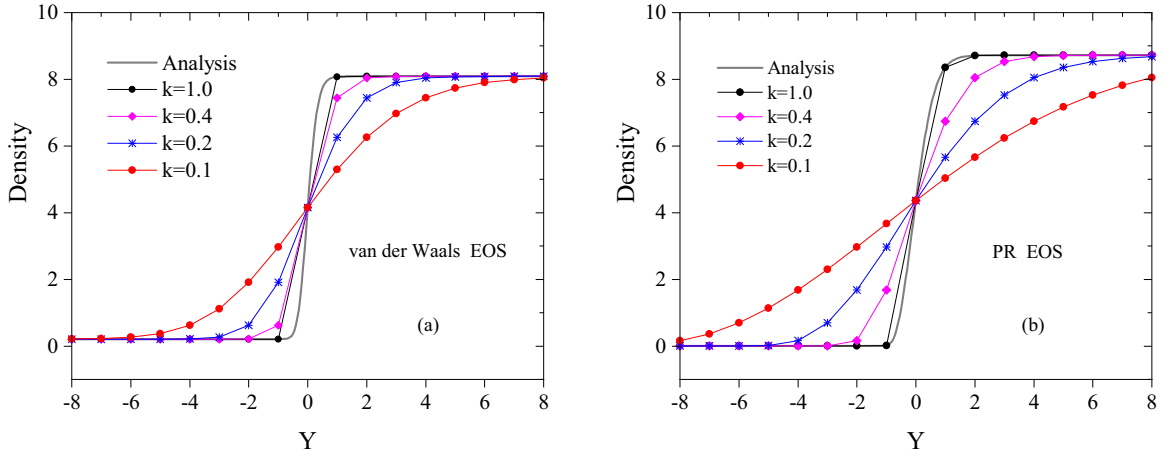

FIG. 12. Density profiles of the liquid-gas transition region depicted as discrete nodes in the momentum space and the various computational mesh spaces defined by different proportional coefficients. It is clear that the density profiles become increasingly gentle with decreasing proportionality coefficient.

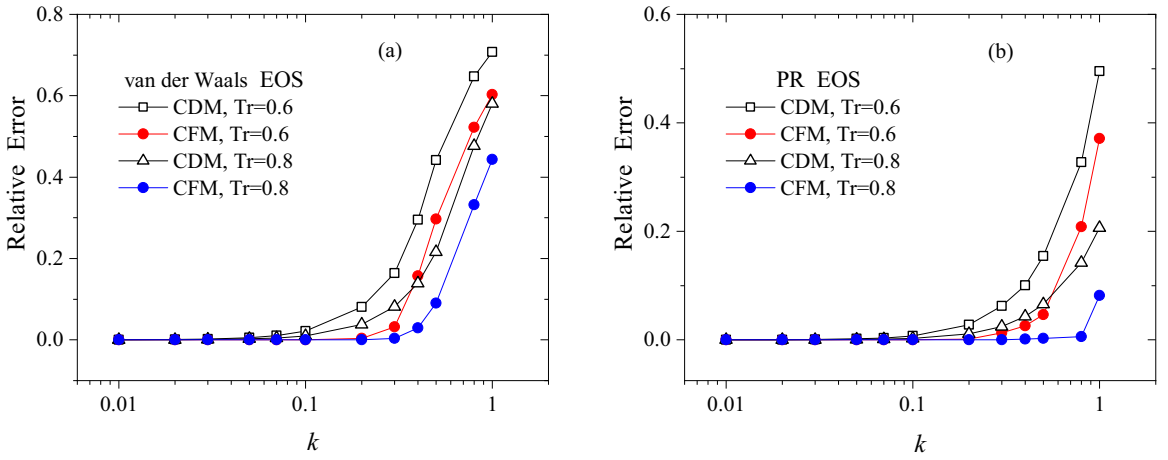

FIG. 13. The relative error of the gradient calculation determined by CDM and CFM against the proportionality coefficient.

were calculated during the whole process. The electric force causes charged side of the droplet to recoil slower than the other side. Thus, the droplet rebounds toward the side which is applied voltage. It can deepen our understanding of the lateral rebound mechanism by electrowetting and help to achieve flexible regulation of droplet impact. In the future work, we will improve the computational efficiency and introduce the more versatile Nernst-Planck model [58]. Moreover, the LB weight stencil will be applied to enhance the isotrop [59,60].

The data that support the findings of this study are available from the corresponding author upon reasonable request.

ACKNOWLEDGMENTS

This work was supported by the National Natural Science Foundation of China (Grants No. 12272100, No. 12062005, No. 81860635, and No. 11862003) and Guangxi Collaborative Innovation Center of Multisource Information Integration and Intelligent Processing.

APPENDIX

Let us consider an isothermal liquid-gas system which has a planar phase interface and develops along the y coordinate. In the equilibrium state, the domain has the boundary conditions $\rho(-\infty) = \rho_g$ and $\rho(+\infty) = \rho_l$. $(\rho_g + \rho_l)/2$ is the origin of the y coordinate. The mechanical equilibrium condition $\nabla \cdot \overleftrightarrow{\mathbf{P}}(\mathbf{x}) = 0$ can be ensured by the equilibrium of the chemical potential $\mu(\mathbf{x}) = \mu_b$ where μ_b is the bulk chemical potential. Solving Eq. (8) in the one-dimensional system gives

$$\frac{\kappa}{2}\left(\frac{d\rho}{dy}\right)^2 = \psi(\rho) - \psi(\rho_b) - \mu_b(\rho - \rho_b), \tag{A1}$$

where ρ_b is equal to ρ_g or ρ_l. Transforming Eq. (A1) and integrating gives

$$\pm\int_{\rho_0}^{\rho} dy = \int_{\rho_0}^{\rho} \frac{d\rho}{\sqrt{\frac{2}{\kappa}\psi(\rho) - \psi(\rho_b) - \mu_b(\rho - \rho_b)}}, \tag{A2}$$

where the sign of the left part is negative for $\rho_b = \rho_g$ in the gas phase or positive for $\rho_b = \rho_l$ in the liquid phase. For a given density $\rho \in [\rho_g, \rho_l]$, integrating Eq. (A2) gives the corresponding y value, and the density distribution with y is then obtained, which is shown as the analysis solution in Fig. 12.

In the present multiphase model, the errors in numerical calculations of multiphase simulations are mainly dependent on the accuracy of the discrete gradient calculations. Denser points make the gradient calculation more accurate. The gradient is calculated using the the central difference method (CDM) and the compact finite-difference method (CFM) respectively. The relative errors of the gradient calculations are shown in Fig. 13. Decreasing the proportionality coefficient can reduce the relative error.

[1] Y. Zhao and Y. Wang, Fundamentals and applications of electrowetting, Rev. Adhes. Adhes. **1**, 114 (2013).
[2] P. Teng, D. Tian, H. Fu, and S. Wang, Recent progress of electrowetting for droplet manipulation: From wetting to superwetting systems, Mater. Chem. Front. **4**, 140 (2020).
[3] Y. Lu, B. Tang, G. Yang, Y. Guo, L. Liu, and A. Henzen, Progress in advanced properties of electrowetting displays, Micromachines **12**, 206 (2021).
[4] T. V. Neumann and M. D. Dickey, Liquid metal direct write and 3d printing: A review, Adv. Mater. Technol. **5**, 2000070 (2020).
[5] Y. Liu and B. Derby, Experimental study of the parameters for stable drop-on-demand inkjet performance, Phys. Fluids **31**, 032004 (2019).
[6] S. Kang, S. Kim, D. K. Sohn, and H. S. Ko, Analysis of drop-on-demand Piezo inkjet performance, Phys. Fluids **32**, 022007 (2020).

[7] F. Perdigones, Lab-on-pcb and flow driving: A critical review, Micromachines **12**, 175 (2021).

[8] S. Paul and H. Moon, Drop-to-drop liquid–liquid extraction of dna in an electrowetting-on-dielectric digital microfluidics, Biomicrofluidics **15**, 034110 (2021).

[9] I. Frozanpoor, M. D. Cooke, V. Ambukan, A. J. Gallant, and C. Balocco, Continuous droplet-actuating platforms via an electric field gradient: Electrowetting and liquid dielectrophoresis, Langmuir **37**, 6414 (2021).

[10] P. Zhao, Y. Li, and H. Zappe, Accelerated electrowetting-based tunable fluidic lenses, Opt. Express **29**, 15733 (2021).

[11] X. Song, H. Zhang, D. Li, D. Jia, and T. Liu, Electrowetting lens with large aperture and focal length tunability, Sci. Rep. **10**, 16318 (2020).

[12] F. Song, B. Ma, J. Fan, Q. Chen, and B. Q. Li, Molecular dynamics simulation on the electrowetting behaviors of the ionic liquid [BMIM][BF_4] on a solid substrate, Langmuir **35**, 9753 (2019).

[13] D. Chakraborty, S. Pathak, and M. Chakraborty, Molecular investigation of contact line movement in electrowetted nanodroplets, Langmuir **36**, 12580 (2020).

[14] S. W. Walker and B. Shapiro, Modeling the fluid dynamics of electrowetting on dielectric (EWOD), J. Microelectromech. Syst. **15**, 986 (2006).

[15] Y. Guan, B. Li, and L. Xing, Numerical investigation of electrowetting-based droplet splitting in closed digital microfluidic system: Dynamics, mode, and satellite droplet, Phys. Fluids **30**, 112001 (2018).

[16] Q. Zhao and W. Ren, A finite element method for electrowetting on dielectric, J. Comput. Phys. **429**, 109998 (2021).

[17] M. Fontelos, G. Grün, U. Kindelan, and F. Klingbeil, Numerical simulation of static and dynamic electrowetting, J. Adhes. Sci. Technol. **26**, 1805 (2012).

[18] R. H. Nochetto, A. J. Salgado, and S. W. Walker, A diffuse interface model for electrowetting with moving contact lines, Math. Models Methods Appl. Sci. **24**, 67 (2014).

[19] H. Aminfar and M. Mohammadpourfard, Lattice Boltzmann method for electrowetting modeling and simulation, Comput. Methods Appl. Mech. Eng. **198**, 3852 (2009).

[20] L. Clime, D. Brassard, and T. Veres, Numerical modeling of electrowetting processes in digital microfluidic devices, Comput. Fluids **39**, 1510 (2010).

[21] H. Li and H. Fang, Hysteresis and saturation of contact angle in electrowetting on a dielectric simulated by the lattice Boltzmann method, J. Adhes. Sci. Technol. **26**, 1873 (2012).

[22] É. Ruiz-Gutiérrez and R. Ledesma-Aguilar, Lattice-Boltzmann simulations of electrowetting phenomena, Langmuir **35**, 4849 (2019).

[23] P. Galliker, J. Schneider, H. Eghlidi, S. Kress, V. Sandoghdar, and D. Poulikakos, Direct printing of nanostructures by electrostatic autofocussing of ink nanodroplets, Nat. Commun. **3**, 1 (2012).

[24] U. N. Tohgha, A. M. Watson, and N. P. Godman, Tuning the electrowetting behavior of quantum dot nanofluids, J. Colloid Interface Sci. **584**, 395 (2021).

[25] B. Zhang, S. Wang, X. He, Y. Yang, X. Wang, and D. Lee, Statics and dynamics of nanodroplet electrowetting on an isothermally heated nanostructured surface, J. Mol. Liq. **342**, 117468 (2021).

[26] A. K. Gunstensen, D. H. Rothman, S. Zaleski, and G. Zanetti, Lattice Boltzmann model of immiscible fluids, Phys. Rev. A **43**, 4320 (1991).

[27] X. Shan and H. Chen, Lattice Boltzmann model for simulating flows with multiple phases and components, Phys. Rev. E **47**, 1815 (1993).

[28] L. Chen, Q. Kang, Y. Mu, Y. He, and W. Tao, A critical review of the pseudopotential multiphase lattice Boltzmann model: Methods and applications, Int. J. Heat Mass Transf. **76**, 210 (2014).

[29] M. R. Swift, W. R. Osborn, and J. M. Yeomans, Lattice Boltzmann Simulation of Nonideal Fluids, Phys. Rev. Lett. **75**, 830 (1995).

[30] Y. Gan, A. Xu, H. Lai, W. Li, G. Sun, and S. Succi, Discrete Boltzmann multiscale modelling of nonequilibrium multiphase flows, J. Fluid Mech. **951**, A8 (2022).

[31] B. Wen, X. Zhou, B. He, C. Zhang, and H. Fang, Chemical-potential-based lattice Boltzmann method for nonideal fluids, Phys. Rev. E **95**, 063305 (2017).

[32] B. Wen, L. Zhao, W. Qiu, Y. Ye, and X. Shan, Chemical-potential multiphase lattice Boltzmann method with superlarge density ratios, Phys. Rev. E **102**, 013303 (2020).

[33] P. L. Bhatnagar, E. P. Gross, and M. Krook, A model for collision processes in gases. I. Small amplitude processes in charged and neutral one-component systems, Phys. Rev. **94**, 511 (1954).

[34] X. He and L. S. Luo, Theory of the lattice Boltzmann method: From the Boltzmann equation to the lattice Boltzmann equation, Phys. Rev. E **56**, 6811 (1997).

[35] P. Lallemand and L. S. Luo, Theory of the lattice Boltzmann method: Dispersion, dissipation, isotropy, Galilean invariance, and stability, Phys. Rev. E **61**, 6546 (2000).

[36] D. d'Humières, Multiple–relaxation–time lattice Boltzmann models in three dimensions, Philos. Trans. Roy. Soc. London. Ser. A: Math. Phys. Eng. Sci. **360**, 437 (2002).

[37] L.-S. Luo, W. Liao, X. Chen, Y. Peng, W. Zhang *et al.*, Numerics of the lattice Boltzmann method: Effects of collision models on the lattice Boltzmann simulations, Phys. Rev. E **83**, 056710 (2011).

[38] S. Girimaji, Lattice Boltzmann method: Fundamentals and engineering applications with computer codes, AIAA J. **51**, 278 (2013).

[39] M. E. McCracken and J. Abraham, Multiple-relaxation-time lattice-Boltzmann model for multiphase flow, Phys. Rev. E **71**, 036701 (2005).

[40] J. S. Rowlinson and B. Widom, *Molecular Theory of Capillarity* (Courier Corporation, Chelmsford, MA, 2013).

[41] T. Lee and P. F. Fischer, Eliminating parasitic currents in the lattice Boltzmann equation method for nonideal gases, Phys. Rev. E **74**, 046709 (2006).

[42] Z. Guo, C. Zheng, and B. Shi, Discrete lattice effects on the forcing term in the lattice Boltzmann method, Phys. Rev. E **65**, 046308 (2002).

[43] P. J. Dellar, An interpretation and derivation of the lattice Boltzmann method using Strang splitting, Comput. Math. Appl. **65**, 129 (2013).

[44] A. L. Kupershtokh, D. A. Medvedev, and D. I. Karpov, On equations of state in a lattice Boltzmann method, Comput. Math. Appl. **58**, 965 (2009).

[45] I. Ginzbourg and P. Adler, Boundary flow condition analysis for the three-dimensional lattice Boltzmann model, J. Physique II **4**, 191 (1994).

[46] N. Cao, S. Chen, S. Jin, and D. Martinez, Physical symmetry and lattice symmetry in the lattice Boltzmann method, Phys. Rev. E **55**, R21 (1997).

[47] X. He, L. Luo, and M. Dembo, Some progress in lattice Boltzmann method. Part I. Nonuniform mesh grids, J. Comput. Phys. **129**, 357 (1996).

[48] J. Theodoor and G. Overbeek, The role of energy and entropy in the electrical double layer, Colloids Surf. **51**, 61 (1990).

[49] K. H. Kang, I. S. Kang, and C. M. Lee, Electrostatic contribution to line tension in a wedge-shaped contact region, Langmuir **19**, 9334 (2003).

[50] J. Hua, L. K. Lim, and C. Wang, Numerical simulation of deformation/motion of a drop suspended in viscous liquids under influence of steady electric fields, Phys. Fluids **20**, 113302 (2008).

[51] J. R. Melcher, *Continuum Electromechanics* (MIT Press, Cambridge, MA, 1981), Vol. 2.

[52] J. Yao, K. Luo, J. Wu, and H. Yi, Electrohydrodynamic effects on bubble dynamics during nucleate pool boiling under the leaky dielectric assumption, Phys. Fluids **34**, 013606 (2022).

[53] H. Huang, M. Krafczyk, and X. Lu, Forcing term in single-phase and Shan-Chen-type multiphase lattice Boltzmann models, Phys. Rev. E **84**, 046710 (2011).

[54] K. H. Kang, I. S. Kang, and C. M. Lee, Geometry dependence of wetting tension on charge-modified surfaces, Langmuir **19**, 6881 (2003).

[55] F. Mugele and J.-C. Baret, Electrowetting: From basics to applications, J. Phys.: Condens. Matter **17**, R705 (2005).

[56] F. Mugele and J. Buehrle, Equilibrium drop surface profiles in electric fields, J. Phys.: Condens. Matter **19**, 375112 (2007).

[57] J. Buehrle, S. Herminghaus, and F. Mugele, Interface Profiles Near Three-Phase Contact Lines in Electric Fields, Phys. Rev. Lett. **91**, 086101 (2003).

[58] R. Eisenberg and D. Chen, Poisson-Nernst-Planck (PNP) theory of an open ionic channel, in *Biophysical Journal* (Biophysical Society, Bethesday, MD, 1993), Vol. 64, pp. A22–A22.

[59] S. P. Thampi, S. Ansumali, R. Adhikari, and S. Succi, Isotropic discrete Laplacian operators from lattice hydrodynamics, J. Comput. Phys. **234**, 1 (2013).

[60] K. Ji, A. M. Tabrizi, and A. Karma, Isotropic finite-difference approximations for phase-field simulations of polycrystalline alloy solidification, J. Comput. Phys. **457**, 111069 (2022).